Journal of Catalysis 257 (2008) 43–54

Contents lists available at ScienceDirect

Journal of Catalysis

www.elsevier.com/locate/jcat

Effect of Zn addition on the water–gas shift reaction over supported palladium catalysts

Luis Bollmann[a], Joshua L. Ratts[a], Ajay M. Joshi[a], W. Damion Williams[a], Jorge Pazmino[a], Yogesh V. Joshi[a], Jeffrey T. Miller[b], A. Jeremy Kropf[c], W. Nicholas Delgass[a], Fabio H. Ribeiro[a,*]

[a] School of Chemical Engineering, Purdue University, 480 Stadium Mall Drive, West Lafayette, IN 47907-2100, USA
[b] BP Research Center, E-1F, 150 W. Warrenville Rd., Naperville, IL 60563, USA
[c] Chemical Technology Division, Argonne National Laboratory, 9700 S. Cass Avenue, Argonne, IL 60439, USA

ARTICLE INFO

Article history:
Received 31 January 2008
Revised 3 April 2008
Accepted 4 April 2008
Available online 22 May 2008

Keywords:
Water–gas shift
Methanation
Palladium catalysts
Fuel cells
Zinc oxide
Catalyst promoters
Kinetics
Pd–Zn alloys
In situ IR spectroscopy
EXAFS

ABSTRACT

The effect of Zn addition on the Pd turnover rate (TOR) for the water–gas shift (WGS) reaction was studied on 2 wt% Pd on alumina with Zn content varying from 0 to 19% Zn by weight. Over 85% of the Zn reacted with alumina to form zinc aluminate with a fraction reacting with Pd. The average Pd–Zn coordination number as measured by extended X-ray absorption fine structure (EXAFS) increased monotonically from 0 to 4.5 as the Zn loading on alumina increased. At a loading of 2% Pd and 19% Zn on alumina the molar fraction of Zn in the Pd particles was 0.34, and the turnover rate increased by a factor of 13, as compared with the pure metallic Pd supported on alumina, to 3.6×10^{-2} mol H_2 s^{-1} (mol exposed Pd)$^{-1}$ at 280 °C, 6.8% CO, 8.5% CO_2, 21.9% H_2O, and 37.4% H_2 at 1 atm. The formation of the ordered 1:1 PdZn intermetallic compound by deposition of Pd on zinc oxide increased the average Pd–Zn coordination number to 5.9 and the WGS turnover rate by a factor of 20 to 5.3×10^{-2} mol H_2 s^{-1} (mol exposed Pd)$^{-1}$. The bonding of adsorbed CO changed from 80% bridging on pure Pd to 90% linear on the 1:1 PdZn intermetallic compound as determined by diffuse reflectance infrared spectroscopy performed under WGS conditions. The fraction of CO binding linearly to Pd correlated linearly with the WGS rate per Pd on the surface. Because the dispersion of the samples was about the same, this result implies that the number of active sites can be counted by the fraction of CO binding linearly. A simple random substitution model for PdZn distribution was used to estimate the concentration of Pd and Zn on the surface, based on the coordination numbers measured by EXAFS. The correlation of the reaction rate with the types of sites on catalysts with six different Pd–Zn compositions shows that the data is consistent with an active site composed of surface Pd atoms with surface coordination to 2 Pd and 4 Zn atoms, which is the coordination expected for the (111) plane of the 1:1 PdZn intermetallic compound. An alternate explanation for the promotional effect of Zn on Pd/alumina is that the formation of zinc aluminate breaks a deleterious Pd–alumina interaction.

1. Introduction

Interest in fuel cell research has flourished in recent years due to the possible application of fuel cells in mobile or domestic power generation [1]. The areas of hydrogen generation and CO purification have attracted much interest. In both areas, the water–gas shift (WGS) reaction ($CO + H_2O \rightarrow CO_2 + H_2$) plays an important role [2]. Commercially available $Cu/ZnO/Al_2O_3$ catalysts have the highest rate per unit of volume but suffer from poor stability under constant startup-shutdown conditions and at high temperatures [3]. Therefore, attention has been given to supported noble metals such as Pt and Pd [4–9]. These catalysts are more robust but exhibit lower turnover rates (TOR) than that exhibited by the industrial $Cu/ZnO/Al_2O_3$ catalyst.

In the related field of methanol reforming ($H_3COH + H_2O \rightarrow CO_2 + 3H_2$), the reaction proceeds selectively over Cu catalysts, whereas methanol preferentially decomposes to CO over Pt and Pd catalysts [10,11]. However, the selectivity toward methanol reforming is improved when Pd is supported on ZnO [12–22]. Iwasa and coworkers [16] were the first to observe that Pd/ZnO had a high rate per gram toward methanol reforming with high selectivity toward CO_2, which was attributed to the formation of a PdZn intermetallic compound during the reduction pretreatment of the catalyst at temperatures above 300 °C. Photoelectron spectroscopy and valance band structure calculations showed that on PdZn, the Pd 4d local density of states (LDOS) was similar to the LDOS of Cu [23–26]. Therefore, it was suggested that PdZn could be a good catalyst for other reactions catalyzed by Cu [13].

---

* Corresponding author. Fax: +1 (765) 494 0805.
E-mail address: fabio@purdue.edu (F.H. Ribeiro).

0021-9517/$ – see front matter © 2008 Elsevier Inc. All rights reserved.
doi:10.1016/j.jcat.2008.04.005

Iwasa and coworkers [19] also studied the effect on methanol reforming of Zn addition to supported Pd catalysts. Whereas the addition of Zn to CeO_2- and ZrO_2-supported Pd induced the formation of PdZn during steam reforming, the addition of Zn to SiO_2- and Al_2O_3-supported Pd did not affect its structure. No reduction of Zn or intermetallic formation was observed on the SiO_2 support even at temperatures of 700 °C. Xia et al. [27] studied the activity of Pd/ZnO catalysts supported on high surface area Al_2O_3 for methanol reforming. The Al_2O_3-supported catalysts with low Pd/Zn ratios were less selective toward methanol decomposition to CO than the ZnO-supported sample. Only at Pd loadings $>12\%$ and Pd/Zn molar ratios >0.76 was formation of PdZn observed after reduction in 3% H_2 at 400 °C. *Ab initio* calculations, coupled with X-ray photoelectron spectroscopy measurements, showed that the electronic perturbations caused to the Pd atom by the formation of PdZn reduced the ability of Pd to adsorb CO by transferring electrons from Pd to Zn, which in turn weakened the Pd(4d)–CO($2\pi^*$) bonding interactions [28].

Here we report on the turnover rate of $Pd/Zn/Al_2O_3$ catalysts for the forward WGS reaction at 280 °C and 6.8% CO, 8.5% CO_2, 21.9% H_2O, and 37.4% H_2 at 1 atm total pressure. We investigated the effect of Zn by preparing samples with intermediate loading between pure Pd and the 1:1 PdZn intermetallic compound. The cluster structure was characterized by extended X-ray absorption fine structure (EXAFS) and X-ray diffraction (XRD). Diffuse-reflectance infrared Fourier transform spectroscopy (DRIFTS) measurements were obtained under reaction conditions to study how the addition of Zn affects the adsorption of CO on the surface and how it correlates with the reaction turnover rate.

2. Experimental

2.1. Catalyst preparation

All of the reagents used were obtained from Aldrich except the γ-alumina, which was a high-purity γ-Al_2O_3. The γ-Al_2O_3 had a BET area of 241 $m^2\,g^{-1}$, a pore volume of 0.5 $ml\,g^{-1}$, and an average pore diameter of 7 nm. The supports were calcined at 500 °C before the metal precursors were added. A typical synthesis involved adding 0 to 7 g of $Zn(NO_3)_2{\cdot}6H_2O$ in 3.6 ml of H_2O to 6.0 g of alumina. The sample was dried at 100 °C and calcined at 300 °C for 2 h in flowing air. After 3.4 g of 10% solution of $Pd(NH_3)_4(NO_3)_2$ were added to this support, it was dried at 100 °C, calcined at 300 °C in flowing air for 2 h, and prereduced at 250 °C in H_2 at atmospheric pressure. Identification of the various samples is based on the amount of Pd and Zn; for example, sample 2Pd6Zn is a 2% Pd on Al_2O_3 with 6% Zn loading by weight. In addition, a physical mixture of 2% Pd on Al_2O_3 (2Pd0Zn) and ZnO was prepared. The amount of ZnO added was adjusted until the Zn concentration in the mixture reached 6% by weight. This sample was designated 2Pd6ZnPM. For the ZnO-supported Pd catalyst, 1.75 g of a 10% solution of $Pd(NH_3)_4(NO_3)_2$ was added to 6.0 g of ZnO (14 $m^2\,g^{-1}$ and 0.04 $cm^3\,g^{-1}$). The solid was dried at 100 °C, calcined at 250 °C in flowing air for 2 h, and then prereduced at 250 °C in H_2 at atmospheric pressure; the resulting sample is designated 1PdZnO. The actual Pd and Zn weight loadings for all samples were verified by inductively coupled plasma atomic emission spectrometry (ICP-AES).

2.2. Catalyst characterization

2.2.1. O_2 and H_2 chemisorption measurements

The chemisorption properties of the used catalysts were determined with a H_2–O_2 titration method [29,30] in a standard volumetric apparatus at 100 °C in the pressure range of 50–180 Torr. The catalysts (0.35–0.50 g) were dried in open air at 150 °C for 12 h before being transferred to the apparatus, after which they were reduced at 300 °C for 30 min under 33 $ml\,min^{-1}$ of flowing H_2. The temperature was then reduced to 100 °C, and the system was evacuated. First, O_2 chemisorption was performed. Then the system was evacuated and H_2 titration was done. Finally, the BET area was measured at LN_2 temperature. For sample 2Pd19Zn, the Pd dispersion also was measured by H_2 chemisorption after reduction at 300 °C for 4 h.

2.2.2. Powder X-ray diffraction (XRD)

Powder XRD patterns were collected in air on a Scintag X2 diffractometer with a θ–θ setup. The patterns were collected between the 2θ angles of 25 and 50 degrees in 0.04-degree steps. The collection time per step was 30 s.

2.2.3. Diffuse reflectance infrared Fourier transform spectroscopy (DRIFTS) studies

The Spectra-Tech DRIFTS cell and FTIR spectrometer used in this study have been described elsewhere [9]. All presented spectra were collected at a resolution of 4 cm^{-1} and averaged over 32 scans. For the *in situ* studies, CO, H_2, CO_2, and N_2 were bubbled through a H_2O saturator heated to a temperature at which the vapor pressure gave the desired concentration. The total flow was maintained at 50 sccm, and all lines were heat-traced with heating tape and covered with insulation and aluminum foil to prevent condensation of the water vapor.

The diffuse reflectance (DR) spectra are presented in absorbance units defined as

$$\mathrm{Abs} = \log\left(\frac{1}{R_\infty}\right), \tag{1}$$

where R_∞ is as defined by Phatak et al. [9]. Although we realize that these are not true absorbance values, because we are collecting diffusely reflected infrared radiation, we refer to them as absorbance units from here on. Absorbance units were used due to the findings of a recent study by Sirita et al. [31] that compared the use of both absorbance and Kubelka–Munk units for quantitative analysis of CO adsorption on a Pt/SiO_2 catalyst and found that absorbance units gave the most appropriate representation of adsorbate surface concentration for reflectance values >0.6. All spectra presented in our study had reflectance values >0.6 at the peak maximum for CO adsorption, and thus absorbance units were used.

The catalysts loaded into the DRIFTS cell were the used catalysts from the kinetic study. They were pretreated by first heating in flowing N_2 to 150 °C and holding for 15 min. The temperature was then increased to 300 °C at a constant rate of $\sim 8\,°C\,min^{-1}$. Once at 300 °C, the catalyst was exposed to 10 min of 10% O_2, followed by a 4-min nitrogen purge and 30 min of 25% H_2. Once the cell was purged of H_2, the temperature was decreased to 100 °C in N_2 for various CO adsorption experiments (results not presented). The catalyst was then heated to 280 °C at a constant rate of $\sim 8\,°C\,min^{-1}$ and exposed to H_2O vapor by bubbling 50 sccm N_2 through the heated saturator. Once the single-beam background had stabilized, a 256-scan background was collected, and the catalyst was exposed to the complete WGS mixture of 6.8% CO, 11% H_2O, 8.5% CO_2, 37.3% H_2, and N_2.

Deconvolution of the DR spectra was completed with CasaXPS version 2.3.12. Once the data were collected, the spectra were baseline-corrected with a linear background from 2144 cm^{-1} (Q branch of gas-phase CO) to ~ 1700 cm^{-1}. The region of interest for peak deconvolution was the area at which CO adsorbs on Pd. However, the gas-phase CO spectrum partially overlaps the region of linear CO on Pd. We attempted to subtract the gas-phase CO bands with a reference spectrum of CO flowing over an alumina sample at room temperature (RT), but the shape of the gas-phase spectrum collected under WGS conditions at 280 °C was not the same as that of the reference. To remedy this, we used a pure Gaussian curve to simulate the P branch of the gas-phase CO spectrum. Compared with the reference spectrum, the Gaussian curve captured the shape of the lower wavenumber side of the P branch, as shown in Fig. 4. Thus, we believe that this methodology for subtracting out the gas-phase CO spectrum is sufficient for quantifying the adsorbed CO peaks.

The region set for deconvolution for the Pd/Al_2O_3 and $Pd/Zn/Al_2O_3$ catalysts was 2144–1674 cm^{-1}, and that for the Pd/ZnO catalyst was 2144–1809 cm^{-1}. Pure Gaussian curves were added to represent the different identified species. Due to the asymmetric shape of the lower wavenumber side of linearly bound CO on Pd, an extra peak was added to complete the fit. The peak positions, areas, and their full widths at half maximum (FWHM) were then optimized by minimizing the root mean squared error (RMSE) through Marquardt iterations completed by CasaXPS. Once a physically reasonable fit was obtained, constraints were put on the positions such that the peaks could not be moved out of their respective regions. The constrained peaks were then applied to the whole data set, and the RMSE was minimized. For the RMSE minimization on the whole set, the only constraint was that of the aforementioned position. The linearly bound CO species were allowed to vary by $\sim \pm 5$ cm^{-1}; the bridging CO species, by $\sim \pm 30$ cm^{-1}. The FWHM values were not constrained, but were monitored such that a reasonable fit was obtained.

2.2.4. Pd-edge extended X-ray absorption fine structure (EXAFS) measurements

X-ray absorption measurements were made on the insertion-device beam line of the Materials Research Collaborative Access Team (MRCAT) at the Advanced Photon Source, Argonne National Laboratory. Measurements were made in transmission mode with the ionization chambers optimized for the maximum current with linear response ($\sim 10^{10}$ photons detected s^{-1}) using a mixture of N_2 and He in the incident X-ray detector and a mixture of ca. 20% Ar in N_2 in the transmission X-ray detector. A third detector in the series collected a Pd foil spectrum simultaneously with each measurement for energy calibration. Catalyst samples were pressed into a cylindrical holder with a thickness chosen to give a total absorbance (μx) at the Pd K (24.350 keV) edge of about 2.0 and a Pd edge step ($\Delta \mu x$) of ca. 0.5. Unless stated otherwise, the Pd catalysts used in the kinetic experiments were re-reduced at 300 °C for 30 min in 4% H_2/He followed by He purge at 300 °C, and cooled to RT in a continuous-flow EXAFS reactor cell. The spectra were obtained at RT under static He atmosphere. Phase shifts, backscattering amplitudes, and XANES references were obtained from Pd foil for Pd–Pd. For Pd–Zn, the phase and amplitude files were theoretical from FEFF. Standard procedures based on WINXAS97 software were used to extract the EXAFS data. The coordination parameters were obtained by a least square fit in q- and r-space of the isolated nearest-neighbor, k^2-weighted Fourier transform data. The data fit equally well with both k^1 and k^3 weightings.

2.3. Kinetic measurements

The kinetic measurements were obtained in a unit comprising four parallel plug flow reactors (PFR), each housed inside a separate tubular furnace to control the temperature independently. The gases were fed to the reactors with eight mass flow controllers. Four of these mass flow controllers were used to control the composition of the gases (Ar, CO, CO_2 and H_2) in the main gas feed, and the other four were used to regulate the flow of the main premixed feed to each reactor. High-purity CO was preheated to 320 °C on a Cu turnings-filled trap before it entered the reactor to decompose the Fe-carbonyls, which otherwise can be deposited on the catalyst surface, affecting the measured rates. High-purity H_2 was passed through a Deoxo trap. Deionized water was metered by a positive displacement pump and was vaporized before entering the reactor. To avoid fluctuations in the water partial pressure, a 0.254-mm-i.d. capillary tube was used to deliver the water. After each reactor, a condenser chilled the gases to 0 °C to maintain a low and constant partial pressure of water. A network of valves allowed the periodic injection of the gas streams coming from all four reactors into an Agilent 6890 gas chromatograph (GC) equipped with a thermal conductivity detector (TCD) and a Carboxen 1000 column. The inlet gases were analyzed before each injection to ensure precise measurement. In general, the rate of CO consumption was used as the WGS rate. In the cases where methane was detected by the GC, the WGS rate was calculated by subtracting the rate of methane formation from the total rate of CO consumption. The carbon mass balance was >96%. The reactor temperatures were adjusted to keep the conversion of all the gases below 10%, thereby maintaining differential conditions. The total inlet flow rate was held constant at 75.4 $ml\,min^{-1}$, with a standard inlet gas composition of 6.8% CO, 8.5% CO_2, 21.9% H_2O, 37.4% H_2, and balance Ar, which was used as an internal standard. This gas composition mimics that seen at a fuel reformer outlet.

Table 1

Summary of catalyst metal loading and O_2–H_2 titration results

Catalyst	Metal content[a]		O_2–H_2 titration[b]		Pd dispersion[b]	Surface Zn/Pd ratio[c,d]
	Pd (wt%)	Zn (wt%)	O_2 uptake ($\mu mol\,g^{-1}$)	H_2 uptake ($\mu mol\,g^{-1}$)		
2Pd0Zn	2.3	0	20 ± 1	75 ± 3	0.24 ± 0.01	–
2Pd2Zn	2.3	2.5	34 ± 1	91 ± 3	0.27 ± 0.01	0.2
2Pd6Zn	2.1	6.2	45 ± 1	87 ± 3	0.29 ± 0.01	0.5
2Pd6Zn 500[e]	2.1	6.2	51 ± 1	73 ± 3	0.24 ± 0.01	1.0
2Pd6ZnPM	1.9[f]	5.9[f]	29 ± 1	86 ± 3	0.32 ± 0.01	0.1
2Pd6ZnPM 500[e]	1.9[f]	5.9[f]	63 ± 1	76 ± 3	0.28 ± 0.01	1.3
2Pd10Zn	2.0	9.5	49 ± 1	76 ± 3	0.27 ± 0.01	0.9
2Pd14Zn	2.0	13.7	38 ± 1	66 ± 3	0.24 ± 0.01	0.7
2Pd19Zn	2.0	19.0	39 ± 1	23 ± 3	0.20 ± 0.02[g]	3.6
1PdZnO	1.0	–	23 ± 1	27 ± 3	0.19 ± 0.02	1.4

[a] Metal content as measured by ICP-AES.

[b] Titration and dispersion measurements done on catalysts after WGS reaction.

[c] Ratio obtained from O_2–H_2 titration data assuming that oxygen adsorbed on Pd and Zn, while hydrogen only reacted with oxygen adsorbed on Pd. Oxygen coverage on the Pd and Zn surfaces were assumed to be 0.74 and 1 monolayers, respectively.

[d] Zn/Pd ratio includes Zn atoms both on the surface of Pd particles and on the surface of the support.

[e] Samples reduced under 25% H_2/75%Ar for 2 h at 500 °C.

[f] Weight loading calculated based on addition of 0.04 g ZnO to 0.5 g 2Pd0Zn.

[g] Pd dispersion measured by H_2 chemisorption.

The temperature was varied over a range of 40 °C, with the concentrations kept at standard conditions, to determine the apparent activation energy. Reaction orders with respect to the reactants and products were measured by varying one gas concentration at a time. The four concentrations were varied over the ranges 4–21% CO, 5–25% CO_2, 11–34% H_2O, and 14–55% H_2. Before the start of the experimental program, the catalysts were reduced by flowing 50 $ml\,min^{-1}$ of 25% H_2/75% Ar mixture at 300 °C for 2 h and stabilized at standard reaction conditions at 350 °C for 12 h. At the end of the experimental program, the reactors were cooled to RT under a 15-$ml\,min^{-1}$ Ar flow. Once at RT, the catalysts were passivated by switching the gas composition to 1% O_2 for 1 h.

3. Results

3.1. Catalyst characterization

Table 1 contains the results from the ICP-AES, O_2 chemisorption and O_2–H_2 titration measurements after reaction. The actual

Pd and Zn loadings were close to the values targeted during synthesis. In all $Pd/Zn/Al_2O_3$ samples, the nominal molar ratio Zn/Pd was always >1. For sample 2Pd2Zn, the nominal ratio was 1.8. This ratio increased to 15.4 for sample 2Pd19Zn. Thus, sufficient Zn was available on the catalyst to react with all of the Pd and form the 1:1 PdZn alloy reported by others [20,27,32,33].

The dispersion of Pd particles was calculated using the O_2–H_2 titration data, assuming that 3/2 mol of H_2 reacted with 1 mol of Pd–O as suggested in the literature [29,30]. In the case of the pure Pd/Al_2O_3 sample, O_2 chemisorption gave similar Pd surface area as the O_2–H_2 titration measurement. All samples except the Pd catalysts with 19% Zn had similar dispersions, ranging from 0.19 to 0.32. The 19% Zn sample had a Pd dispersion of 0.08. However, when H_2 chemisorption was used, the Pd dispersion for the 19% Zn sample increased to 0.20. The reduction temperatures of 300 and 500 °C affected the Pd dispersion only slightly, as shown by the dispersion values for the pairs 2Pd6Zn/2Pd6Zn500 and 2Pd6ZnPM/2Pd6ZnPM500, where the 500 suffix indicates the reduction temperature of 500 °C. The O_2–H_2 titration data for the Al_2O_3-supported Pd catalyst (2Pd0Zn) showed a H_2/O_2 ratio of 3.8, in disagreement with the theoretical ratio of 3.0. Two previous studies [34,35] reported that the adsorption of oxygen on a Pd film saturated at coverage between 0.62 and 0.74 monolayers. Corrected for the submonolayer coverage of O_2, the theoretical H_2/O_2 ratio would be between 3.4 and 3.6, which can explain, at least in part, the higher H_2/O_2 ratio observed experimentally. For the remaining samples, the H_2/O_2 ratio decreased with Zn loading and reduction temperature. Chemisorption data (not shown) on all fresh catalysts before WGS reaction showed an approximate twofold greater Pd dispersion compared with the used samples. The surface Zn/Pd ratio was estimated from the H_2 and O_2 uptake, assuming that oxygen adsorbed on Pd and Zn, whereas on the titration, hydrogen reacted only with oxygen adsorbed on Pd. Oxygen coverage on the Pd and Zn surfaces were assumed to be 0.74 and 1 monolayer, respectively (Table 1).

Fig. 1a shows the diffraction patterns of the $Pd/Zn/Al_2O_3$ catalysts in air after the O_2–H_2 titration measurements. For comparison, the diffraction pattern of the Al_2O_3 support is also shown. Sample 2Pd0Zn showed a peak at 39.9°, attributed to metallic Pd [36]. The relative intensity of the second Pd peak at 46° was too low to be resolved. On addition of Zn on the alumina samples, two new peaks increasing in intensity with Zn loading appeared at 31.7° and 37.3°. These peaks have been identified as belonging to the $ZnAl_2O_4$ structure [37]. For sample 2Pd19Zn, three additional peaks were observed at 32.2°, 34.9°, and 36.8°, attributed to hexagonal ZnO [38]. To quantify the amount of $ZnAl_2O_4$ present in each sample, the XRD findings for Al_2O_3, Pd, $ZnAl_2O_4$ and ZnO were deconvoluted, and the areas under the peaks were calculated. Before deconvolution, the intensity patterns for all samples were scaled such that the intensity in the region in which no diffraction peaks were observed ($2\theta < 27°$) was the same for all samples. Fig. 2 shows the area under the $ZnAl_2O_4$ peak at 31.7° as a function of Zn loading. The amount of $ZnAl_2O_4$ as measured by XRD increased linearly with the amount of Zn added to the catalyst. Fig. 2 also shows the BET area of the $Pd/Zn/Al_2O_3$ samples after WGS reaction. For comparison, the pure Al_2O_3 support had an area of 241 $m^2\,g^{-1}$. The surface area decreased linearly with the amount of Zn added to the support. The largest loss of surface area—a 33% decrease—was observed for the Pd/19% Zn catalyst. The BET areas of the fresh catalysts (data not shown) also decreased linearly with Zn loading.

None of the Pd catalysts supported on Al_2O_3 showed an XRD peak belonging to the PdZn alloy. By comparison, Fig. 1b shows that the Pd catalyst supported on ZnO was the only sample to have a PdZn alloy as detected by XRD. The peaks observed at 41.4° and 44.2° belong to a 1:1 PdZn alloy with the face-centered tetragonal structure of CuAu ($L1_0$-type, space group P4/mmm) with unit cell parameters $a = 4.100$ Å and $c = 3.295$ Å [39,40]. This PdZn intermetallic compound has a bulk Pd–Zn coordination number of 8 and a Pd–Pd coordination number of 4, for a bulk Pd–Zn-to-Pd–Pd coordination number ratio of 2.

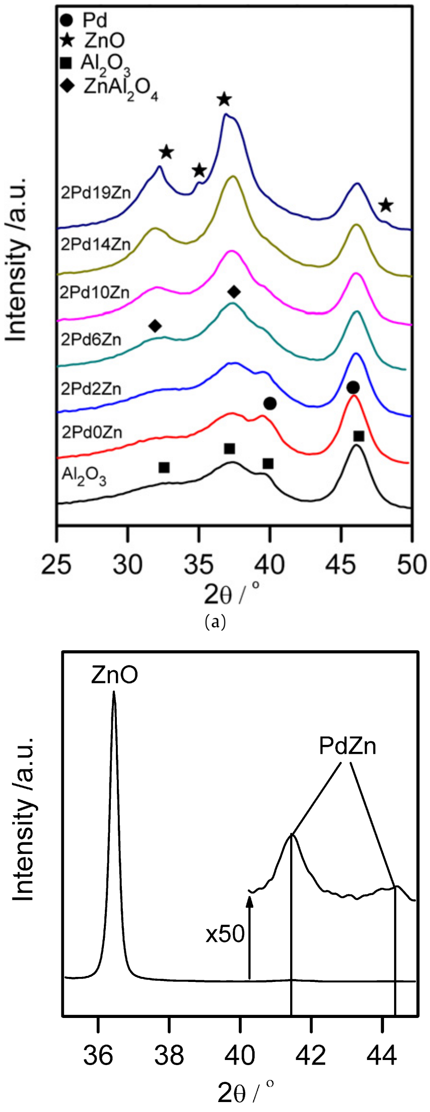

(a)

(b)

Fig. 1. X-ray diffraction patterns in air after O_2–H_2 titration. The curves have been shifted for clarity. (a) $Pd/Zn/Al_2O_3$ catalysts with different Zn loadings. (b) Pd/ZnO.

The diffraction patterns collected for the fresh, prereduced catalysts before WGS reaction showed the diffraction peaks corresponding to the $ZnAl_2O_4$ phase. The Pd diffraction peaks were difficult to separate from the background because of the small Pd particle size.

3.2. EXAFS of reduced catalysts after WGS reaction

The catalysts after reaction were reduced at 300 °C with 4% H_2/96% He, flushed with He, and cooled to RT under He. The spectra were taken at RT and under static He. Fig. 3 shows the k^2-weighted Fourier transform of the EXAFS $\chi(k)$ function for samples 2Pd0Zn, 2Pd2Zn, and 1PdZnO. The pure Pd sample showed two distinct peaks at distances of $R = 2.05$ and 2.50 Å. The intensity ratio of these peaks was independent of particle size. The data for the ZnO-supported Pd had a peak at a lower distance of $R = 2.17$ Å, with a small shoulder at 2.82 Å. The data for the 2%

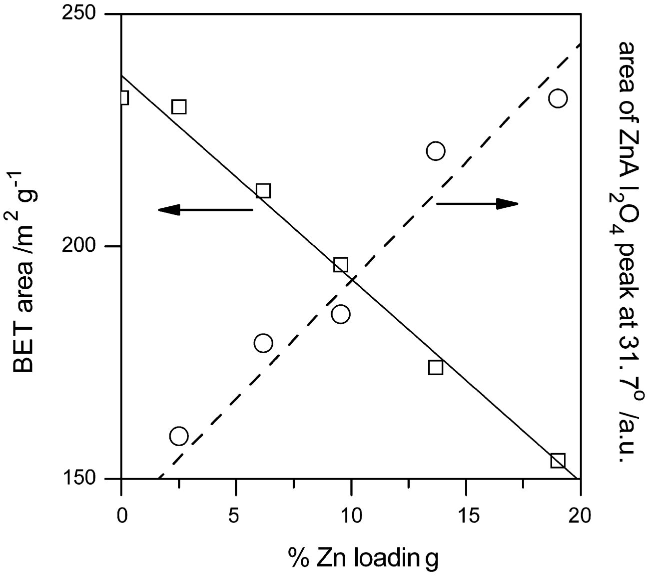

Fig. 2. Experimental BET surface area (□) and area of XRD zinc aluminate peak (○) after WGS reaction (280 °C, 6.8% CO, 8.5% CO_2, 11% H_2O, 37.4% H_2, and balance N_2).

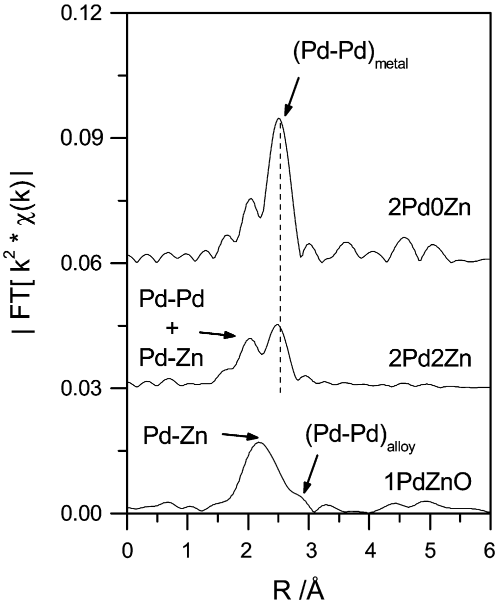

Fig. 3. Pd edge EXAFS of 2% Pd/Al_2O_3 (2Pd0Zn), 2% Pd/2% Zn/Al_2O_3 (2Pd2Zn) and 1% Pd/ZnO (1PdZnO) after reduction on 4% H_2 in He. Data collected at room temperature under He atmosphere.

Table 2
Summary of coordination number (N), bond distance (R), Debye–Waller factor (DWF) and energy correction factor (E_o) obtained from EXAFS measurements

Composition	Scatter	N	R (Å)	DWF ($\times 10^3$)	E_o (eV)
2Pd0Zn	Pd–Pd	11.1	2.75	1.0	2.8
2Pd2Zn	Pd–Zn	2.3	2.54	3.0	−7.9
	Pd–Pd	6.1	2.73	3.0	2.0
2Pd6Zn	Pd–Zn	3.4	2.54	3.0	−8.0
	Pd–Pd	2.9	2.73	3.0	1.5
2Pd10Zn	Pd–Zn	3.7	2.54	3.0	−6.5
	Pd–Pd	2.4	2.73	3.0	0.5
2Pd14Zn	Pd–Zn	3.8	2.55	3.0	−6.9
	Pd–Pd	2.2	2.73	3.0	−0.9
2Pd19Zn	Pd–Zn	4.5	2.54	3.0	−6.8
	Pd–Pd	1.8	2.73	3.0	−3.6
1PdZnO	Pd–Zn	5.9	2.57	3.0	−4.3
	Pd–Pd	2.9	2.88	3.0	3.3

Zn sample showed two peaks, both at similar positions as the pure Pd/Al_2O_3 sample. However, the peak intensity ratio was different suggesting that the peak at $R = 2.05$ Å had a contribution from another peak. The EXAFS data for the 6%, 10%, 14% and 19% Zn samples showed contributions from the same peaks at 2.05 Å and 2.5 Å as the 2% Zn sample. The coordination parameters were obtained by fitting one coordination shell for the Pd–Zn neighbors and 2 coordination shells for the Pd–Pd neighbors. The reason for including 2 coordination shells for Pd–Pd neighbors was that the Pd–Pd nearest neighbor distance is different in pure metallic Pd particles compared with intermetallic 1:1 PdZn particles. Based on the crystal structure, the Pd–Pd distance in the intermetallic is 0.15 Å larger than in the metallic particles. The fitting results are shown in Table 2. The pure Pd catalyst supported on Al_2O_3 had only Pd–Pd neighbors, as would be expected with a coordination number of 11.1. The fitted Pd–Pd bond distance was 2.75 Å, in agreement with the bond distance calculated from the crystal structure parameters of Pd.

For the Pd/Zn/Al_2O_3 samples, the best fits to the EXAFS data were obtained only when the metallic Pd–Pd shell was included along with the Pd–Zn shell. The resulting bond distances were 2.54 Å for Pd–Zn and 2.73 Å for Pd–Pd. The Pd–Zn distance is shorter than the 2.63 Å Pd–Zn distance obtained from the crystal structure of the PdZn alloy. Tkachenko et al. [41] also studied the 1:1 PdZn alloy with EXAFS and reported a bond distance of 2.59 Å. In that study, XRD data confirmed the presence of the intermetallic 1:1 PdZn compound as in our case. As shown in Table 2, the Pd–Zn coordination number increased and the Pd–Pd coordination number decreased with increasing addition of Zn. For the physical mixture of Pd/Al_2O_3 and ZnO reduced at 300 °C (2Pd6ZnPM), only Pd–Pd neighbors were detected by EXAFS. The average Pd–Pd coordination and bond distance were 9.7 and 2.74 Å, respectively. From EXAFS data, this sample behaved more like a pure Pd sample (2Pd0Zn) rather than a Pd/6% Zn sample (2Pd6Zn). When the physical mixture was reduced at 500 °C (2Pd6ZnPM500), the Pd–Pd coordination number decreased to 3.5 and the Pd–Zn coordination increased to 3.1. The corresponding bond distances were 2.73 and 2.53 Å. These values were similar to those obtained for sample 2Pd6Zn, which has the same Zn loading, with the Zn added through an incipient wetness method.

From the best fit to the data, the Pd–Zn and intermetallic Pd–Pd coordination numbers for the Pd/ZnO sample were calculated as 5.9 and 2.9, respectively. The Pd–Pd coordination shell was located 2.88 Å away from the central Pd atom. This distance is in good agreement with the Pd–Pd distance of 2.90 Å obtained from the intermetallic 1:1 PdZn crystal structure [40]. In addition, the ratio of the Pd–Zn and Pd–Pd coordination numbers (Pd–Zn/Pd–Pd = 2.0) is identical to the ratio expected from the face-centered tetragonal structure of the 1:1 PdZn intermetallic.

3.3. DRIFTS under WGS conditions

Fig. 4 shows the steady-state DR spectra of the set of Pd/Zn/Al_2O_3 catalysts under WGS reactions (6.8% CO, 11% H_2O, 8.5% CO_2, 37.4% H_2, balance N_2) at 280 °C. These conditions were similar to those for the kinetic measurements in the plug-flow reactors, except for the H_2O concentration, which was lower during the DRIFTS measurements (11% vs 22% H_2O), due to limitations of the experimental setup. The P and R branches of gas-phase CO were visible and centered at ~2115 and 2180 cm^{-1}, respectively. Linear and bridging CO species on Pd also were observed in the

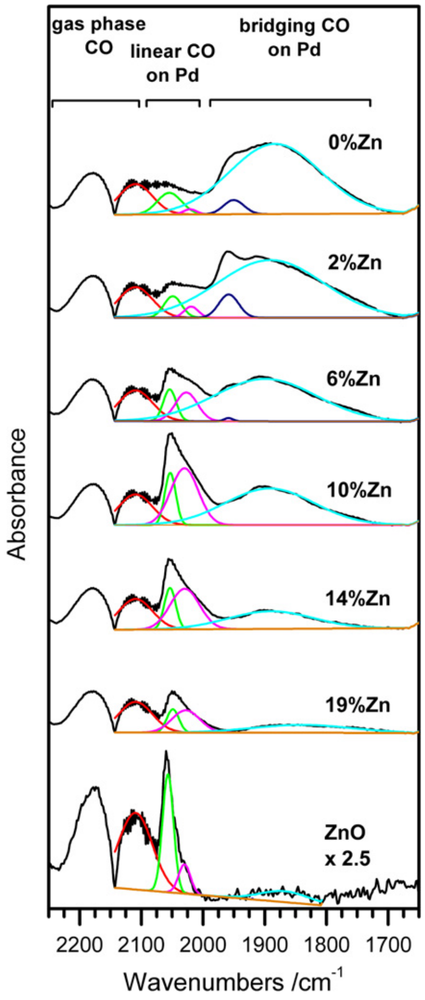

Fig. 4. DRIFTS spectra of Pd/Zn/Al_2O_3 and Pd/ZnO catalysts under WGS conditions (280 °C, 6.8% CO, 8.5% CO_2, 11% H_2O, 37.4% H_2, and balance N_2). Traces for the deconvoluted peaks are included. Data for Pd/ZnO sample has been magnified 2.5 times for clarity.

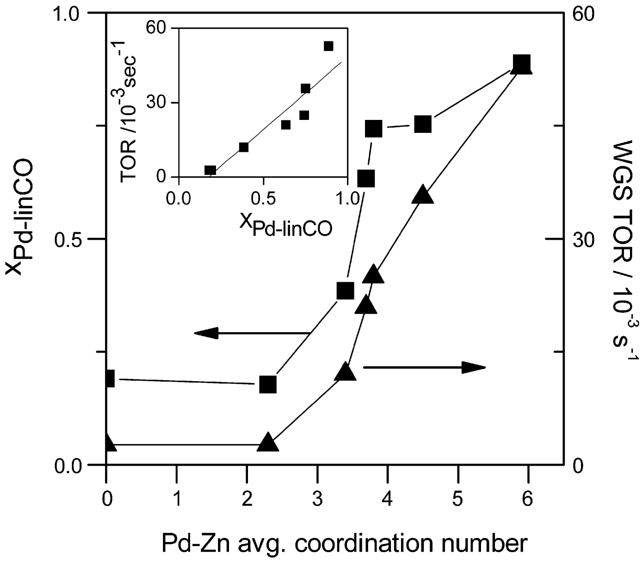

Fig. 5. (■) Fraction of surface Pd that binds CO linearly ($X_{\text{Pd-linCO}}$) under WGS conditions and (▲) WGS TOR as a function of the average Pd–Zn coordination number N_{PdZn} measured by EXAFS. Rates are expressed per exposed mole of Pd and measured at 280 °C and 1 atm (6.8% CO, 8.5% CO_2, 37% H_2O, 37.4% H_2, balance Ar). Inset: correlation between the WGS TOR and $X_{\text{Pd-linCO}}$.

regions 2075–2000 cm^{-1} and 1980–1880 cm^{-1}, respectively [42]. The possibility of three-fold CO species bound to Pd was not excluded because the lower frequency side of the bridge bonded CO peak was not well defined and extended to ~1700 cm^{-1}. But in the present study, which involves the counting of surface Pd atoms, all adsorbed species within this range were assumed to be bridging, because there are no reported values for the extinction coefficient of an adsorbed CO species in threefold or higher coordination.

More specifically, we followed the designations of Choi and Vannice [43], who ascribed the peak centered at ~2060 cm^{-1} to CO linearly bound to Pd and the peaks centered at ~1960 and ~1905 cm^{-1} to CO bridge-bonded to Pd (100) and (111) crystal faces, respectively. The CO band assignment also was in agreement with a recent study that measured the IR frequencies of adsorbed CO on high surface area Pd/ZnO/Al_2O_3 catalysts at RT after exposure to CO [44]. Density functional studies of CO adsorbed on PdZn (111) surface calculated vibrational frequencies of 2026 cm^{-1} and 1872 cm^{-1} for atop and bridging CO, respectively [45]. The next set of peaks between 1600 and 1350 cm^{-1} (Fig. SI1 in Supporting information) indicated the presence of surface species with O–C–O stretching. The peaks at 1592, 1392, and 1376 cm^{-1} follow previous designations by various authors as formate species on the alumina support [46–48]. The bands at 1592 and 1376 cm^{-1} were assigned to the asymmetric and symmetric O–C–O stretching vibration, respectively, whereas the 1392 cm^{-1} was assigned to the C–H deformation mode [46]. We also note the presence of the corresponding C–H vibration and combination C–H bend/O–C–O vibration at ~2900 and ~3000 cm^{-1}, respectively [49]. The rest of the ill-defined peaks between 1592 and 1392 cm^{-1} represent various types of carbonates [50].

After the peak deconvolution was completed, the areas of the two linear CO peaks were added together along with the areas of the two bridge bonded CO peaks. The areas were then divided by their respective integrated absorption coefficient (IAC) reported by Vannice and Wang [51] (6.7×10^7 cm mol^{-1} for linear CO and 35×10^7 cm mol^{-1} for bridging CO) on a Pd/η-Al_2O_3 catalyst and assuming a stoichiometry of 1 CO per Pd atom for linearly bound CO and 1 CO per 2 Pd atoms for bridging CO. The percentage of surface Pd linearly bound to CO then could be calculated. Although the presence of Zn might reduce the IAC for both adsorbed CO species, it was assumed, consistent with the fact that frequencies of the linear and bridge-bonded species do not change much with composition, than the ratio of IACs remains fairly constant compared with the Pd/η-Al_2O_3 sample used in Ref. [51]. The 2% Pd on Al_2O_3 catalyst showed mainly CO adsorbed in the bridged conformation with only 19% of the surface Pd atoms linearly bound to CO. The trend in the fraction of Pd linearly bound to CO as a function of Pd–Zn coordination number is shown in Fig. 5. After addition of 2% Zn, the DR spectra appeared similar to the Zn-free sample with 18% of the surface Pd bound linearly to CO. As more Zn was added, the fraction of Pd linearly bound to CO increased. For the 6%, 10%, 14%, and 19% Zn samples the fraction increased to 0.38, 0.63, 0.74, 0.75, respectively. With 0.89, the Pd supported on ZnO had the largest fraction of Pd bound linearly to CO. For the Pd/Zn/Al_2O_3 catalysts, the area under the carbonate bands increased with increasing Zn loading under WGS conditions. The Pd catalyst supported on ZnO did not shown any bands in the carbonate/formate region (1600–1350 cm^{-1}). One possible reason for the absence of carbonate/formate bands is the surface area of the support, which is 10 times smaller than the support surface area of sample 2Pd19Zn.

Table 3
Summary of kinetic parameters obtained for the production of H_2 on different catalysts at 1 atm total pressure, 6.8% CO, 8.5% CO_2, 21.9% H_2O, 37.4% H_2 and balance Ar

	Temperature[a] (°C)	Apparent E_a ($kJ\,mol^{-1}$)	Apparent reaction orders			
			CO	H_2O	CO_2	H_2
2Pd0Zn	280	82 ± 2	0.38 ± 0.04	0.44 ± 0.05	-0.06 ± 0.01	-0.36 ± 0.04
2Pd2Zn	280	75 ± 2	0.31 ± 0.04	0.61 ± 0.05	-0.07 ± 0.01	-0.36 ± 0.04
2Pd6Zn	285	66 ± 2	0.34 ± 0.04	0.62 ± 0.05	-0.16 ± 0.01	-0.34 ± 0.04
2Pd10Zn	280	68 ± 3	0.38 ± 0.04	0.49 ± 0.05	-0.19 ± 0.01	-0.34 ± 0.04
2Pd14Zn	280	69 ± 3	0.40 ± 0.04	0.59 ± 0.05	-0.25 ± 0.01	-0.29 ± 0.04
2Pd19Zn	275	75 ± 2	0.41 ± 0.04	0.53 ± 0.05	-0.31 ± 0.01	-0.31 ± 0.04
1PdZnO	275	88 ± 2	0.32 ± 0.04	0.45 ± 0.05	-0.27 ± 0.01	-0.26 ± 0.04

[a] Average temperature for the kinetic measurements.

3.4. WGS kinetics of Pd/Zn catalysts

Table 3 shows the apparent activation energies and reaction orders calculated from the kinetic measurements. Because the WGS reaction is reversible, the apparent activation energy and the reaction orders with respect to CO, H_2O, H_2, and CO_2 were fitted to a power rate law expression of the form

$$r = A\exp(-E_{app}/RT)[CO]^a[CO_2]^b[H_2]^c[H_2O]^d(1-\beta), \tag{2}$$

where r is the overall rate, $\beta = ([CO_2][H_2])/(K_{eq}[CO][H_2O])$ is the approach to equilibrium; A and E_{app} are the apparent pre-exponential factor and activation energy for the forward rate; a, b, c, and d are forward reaction orders; and K_{eq} is the equilibrium constant for the WGS reaction. Further details of this analysis have been given by Koryabkina et al. [52]. Figs. 6a and 6b present the kinetic data collected in this study. The standard conditions for the rates reported here were 280 °C and a feed composition of 6.8% CO, 8.5% CO_2, 21.9% H_2O, and 37.4% H_2.

At 280 °C, the CO reaction order was 0.38 for the pure Pd/Al_2O_3 sample. This was larger than that of 0.1 measured for Al_2O_3-supported Pt [9]. In contrast, the H_2O order was lower on Pd than on Pt (0.44 vs 1). The negative reaction orders for CO_2 (−0.06) and H_2 (−0.36) indicates the inhibitory effect of these gases. When the WGS rate was normalized by the number of mol of exposed Pd as measured by the O_2–H_2 titration experiments (Table 1), the pure Pd/Al_2O_3 catalyst had a turnover rate (TOR) of $(2.7 \pm 0.2) \times 10^{-3}$ $mol\,H_2\,s^{-1}$ (mol exposed Pd)$^{-1}$ at 280 °C and an apparent activation energy of 82 ± 2 $kJ\,mol^{-1}$. At temperatures above 280 °C and H_2 concentrations >26%, the formation of methane ($CO + 3H_2 \rightarrow CH_4 + H_2O$) also was observed over the Pd/Al_2O_3 catalyst. Under the same conditions reported for the WGS TOR, the methanation TOR was $(1.2 \pm 0.1) \times 10^{-4}$ $mol\,CH_4\,s^{-1}$ (mol exposed Pd)$^{-1}$. At 2% CO conversion, the catalyst had 95% selectivity toward the WGS reaction.

For the sample 2Pd2Zn (with 2.5% Zn added to the catalyst), the WGS TOR of $(2.6 \pm 0.2) \times 10^{-3}$ $mol\,H_2\,s^{-1}$ (mol exposed Pd)$^{-1}$ was practically the same as the TOR for the pure Pd catalyst. The changes of reaction orders and activation energy between the Zn-free and 2.5% Zn sample were not significant; however, the addition of Zn reduced the formation of methane to below the detection limit of the GC (<3 µmol $CH_4\,L^{-1}$).

On a gradually increase in Zn loading from 2.5 to 19%, the WGS TOR also increased (Fig. 5). As we discuss later when considering potential active sites, the TOR should be the same for all samples when normalized by the proper site. There was a linear relationship between the apparent activation energies for the samples that showed a promotion effect from Zn (Tables 2 and 3) and the average number of Zn to Pd (determined by EXAFS). The apparent activation energy increased from 66 (2Pd6Zn) to 88 $kJ\,mol^{-1}$ (1PdZnO). Another trend was observed in the apparent reaction orders for CO_2, which became more negative as the Zn concentration increased, reaching a minimum value of about −0.31. The apparent orders for CO, H_2O and H_2 demonstrated no systematic trend, and their values remained unchanged as a function of Zn loading.

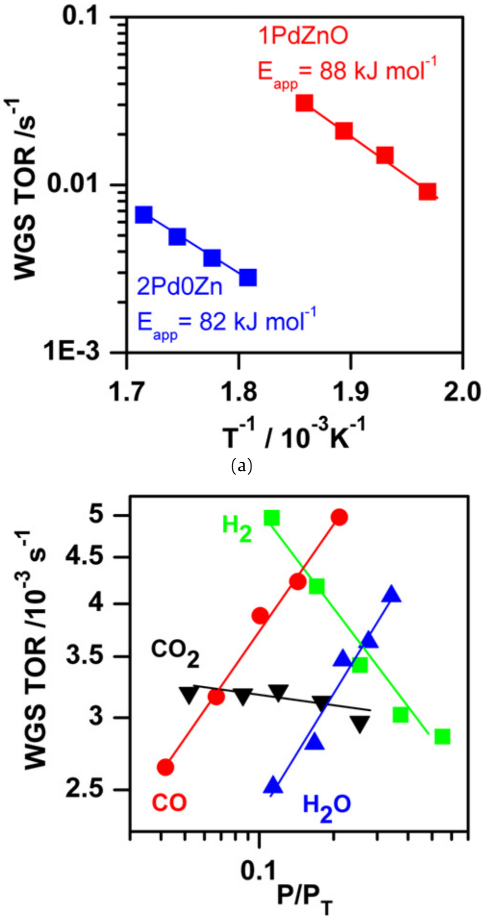

(a)

(b)

Fig. 6. (a) Arrhenius plot for pure Pd catalysts supported on Al_2O_3 (2Pd0Zn) and ZnO (1PdZnO). TOR measured under 6.8% CO, 8.5% CO_2, 37% H_2O, 37.4% H_2 at 1 atm total pressure. (b) Apparent reaction orders for 2Pd0Zn catalyst. Concentrations expressed as partial pressures (P/P_T). TOR measured at 280 °C.

The TOR for the ZnO-supported Pd was $(5.3 \pm 0.8) \times 10^{-2}$ $mol\,H_2\,s^{-1}$ (mol exposed Pd)$^{-1}$. This catalyst had the highest activation energy, 88 ± 2 $kJ\,mol^{-1}$. The CO, H_2O, and H_2 reaction orders on Pd/ZnO were very similar to those for Pd/Al_2O_3 and $Pd/Zn/Al_2O_3$; however, as in those catalysts, the CO_2 reaction order of −0.27 was significantly more negative than the same reaction order for the Pd/Al_2O_3 sample.

Fig. 5 shows the WGS TOR as a function of the Pd–Zn coordination number detected by EXAFS. The difference between the lowest and highest rates was a factor of 20.

The TORs for samples 2Pd6Zn and 2Pd6Zn500 were $(1.2 \pm 0.1) \times 10^{-2}$ and $(1.3 \pm 0.1) \times 10^{-2}$ $mol\,H_2\,s^{-1}$ (mol exposed Pd)$^{-1}$, respectively. The only difference between these samples was the reduction temperature (300 °C and 500 °C, respectively). Catalysts

2Pd6ZnPM and 2Pd6ZnPM500 were physical mixtures of 2% Pd on Al_2O_3 with bulk ZnO. The former was reduced under 25% H_2 at 300 °C, and the latter was reduced at 500 °C. The WGS and methanation TORs for the sample reduced at 300 °C were $(3.1 \pm 0.2) \times 10^{-3}$ mol H_2 s^{-1} (mol exposed Pd)$^{-1}$ and $(1.2 \pm 0.1) \times 10^{-4}$ mol CH_4 s^{-1} (mol exposed Pd)$^{-1}$, respectively, which are similar to the TORs for the pure Pd on Al_2O_3. The behavior of the sample reduced at 500 °C was more like that of sample 2Pd6Zn; the WGS TOR was $(15 \pm 1) \times 10^{-3}$ mol H_2 s^{-1} (mol exposed Pd)$^{-1}$, and the corresponding CH_4 rate was below the detection limit of the GC.

4. Discussion

4.1. WGS kinetics of PdZn alloys

Fig. 5 shows that the TOR of the WGS reaction increased by a factor of 20 as Zn was added to Pd. The data in Tables 2 and 3 show that the apparent activation energy increases linearly as a function of the experimentally measured Pd–Zn coordination number for the samples that showed an enhancement in WGS rate by addition of Zn. The value of E_a corresponding to pure Pd that is obtained by extrapolating the value to zero coordination number is 37 kJ mol^{-1}. Because this is distinct from the experimental value of 82 kJ mol^{-1}, it suggests that the reaction mechanism changes as Zn is added to Pd. Another trend that can be seen is the decreasing apparent order on CO_2, which again indicates a change in the reaction mechanism as Zn is added to Pd. Although the IR data demonstrate the presence of many species between 1700 and 1300 cm^{-1}, including an increase in the number of carbonates as the CO_2 order becomes more negative for the samples supported on alumina, these species are on the support and seem to be spectators. It is surprising that the reaction orders for CO, H_2O, and H_2 show no trend.

Comparing our data with that in the literature, including Grenoble et al. [53], is not straightforward as previous studies did not consider the inhibition effect of the products. As discussed previously [52], not considering these effects will cause the rates, as well as the apparent activation energies and orders, to be incorrect. Assuming a differential plug flow reactor configuration and using the kinetic parameters obtained in our study to calculate the WGS TOR under the conditions reported by Grenoble et al. gave a rate that is a factor of 1.6 lower than what they reported. Although the difference is small, it agrees with the rate inhibition by H_2. In our study, the CO apparent reaction order (0.38) was higher than the CO order (0.14) measured by Grenoble et al., likely because the H_2 inhibition effect was not taken into account.

After the addition of 2% Zn, the WGS TOR of $(2.6 \pm 0.2) \times 10^{-3}$ mol H_2 s^{-1} (mol exposed Pd)$^{-1}$ was practically the same as the TOR for the pure Pd catalyst ($(2.7 \pm 0.2) \times 10^{-3}$ mol H_2 s^{-1} (mol exposed Pd)$^{-1}$). The change of reaction orders between the Zn-free and 2% Zn sample were not significant, indicating that the relative concentrations of surface species did not change significantly for this sample on the addition of Zn. In contrast, the methanation reaction decreased to below the detection limit on the addition of 2% Zn. It is a well-known effect in catalysis that sites that bind most strongly on a surface are the first to be titrated/poisoned. These are probably low-coordination sites necessary to dissociate CO during methanation. Therefore, the Zn on the surface of Pd particles could have blocked the few sites responsible for methanation.

4.2. Structure of the PdZn compounds

Reduction of the catalyst at 300 °C was sufficient to promote Pd alloying with Zn, as verified by EXAFS. In addition, IR data showed that under WGS conditions, Zn was present on the surface of the PdZn particles. But because IR and EXAFS data are averaged over all clusters, which may not have uniform composition, the question regarding the structure of such compounds remains. The XRD data for the ZnO-supported Pd showed the diffraction peaks for an ordered 1:1 PdZn intermetallic. The presence of only the 2.88 Å Pd–Pd bond distance in the EXAFS data and the ratio between the measured Pd–Zn and Pd–Pd coordination of 2 further confirmed the presence of the ordered alloy. For the Pd/Zn/Al_2O_3 samples, the absence of the 1:1 PdZn intermetallic diffraction peaks did not rule out the absence of regions and/or particles with the ordered intermetallic structure but in small enough domains to remain undetected by XRD. The fact that the EXAFS data were best fitted only when the shorter Pd–Pd bond distance typical of metallic Pd was included could suggest that there was no ordered PdZn intermetallic in these samples, but rather Zn atoms were dispersed in the Pd nanoparticles. The trend in rates for the series of samples from PdZn/Al_2O_3 to the Pd/ZnO (where the Pd–Zn coordination number was varied from 2.3 to 5.9) was smooth (Fig. 5) and suggested the presence of homogeneous PdZn particles. For example, the presence of a bimodal distribution with pure Pd (low TOR) and 1:1 PdZn alloys (high TOR) is not consistent with the preparation procedure used for the alumina samples, because the Zn precursor was first dispersed and calcined (probably uniformly, as shown in Fig. 2), after which the Pd salt was added to this uniformly distributed Zn/alumina surface. The presence of pure Pd also would imply the formation of methane, not observed in any of the samples containing Zn.

4.3. Surface composition of PdZn WGS catalysts

The data on O_2–H_2 titration and DRIFTS measurements contain information about the average surface composition but not on the arrangement of the Pd and Zn atoms. To generate more surface-specific information, the formation of the PdZn alloy was simulated by randomly replacing Pd atoms in a nanoparticle with Zn atoms. The simulated particles had a cubo-octahedral geometry with 4 nm from face to face, with a total of 4033 atoms. Of these, 1082 atoms were at the surface with a corresponding dispersion of 0.27. The size of the Pd particle was chosen to match the particle size as determined by O_2–H_2 titration. Using random sampling, Pd atoms were replaced by Zn in 10,000 attempts per nanoparticle. The procedure was repeated four times with different random sequences, and the results were averaged. Because the Pd–Zn bond is stronger than Zn–Zn bonds [28], the substitution was accepted only if the Pd–Pd coordination number of the randomly chosen Pd was larger than its Pd–Zn coordination number. This simple procedure ensured maximum Pd–Zn coordination. No other criteria (e.g., preferential surface presence by Zn due to its lower surface energy) were used to guide the Zn substitution. The displacement of atoms after each substitution to minimize the total configurational energy of the particle also was not attempted. After each substitution, the average Pd–Zn coordination of the particle was calculated. Then, for a particular Pd–Zn coordination experimentally observed by EXAFS, the Pd–Zn coordination of the Pd atoms on the surface of the particle was counted; that is, surface Pd atoms were categorized according to their Pd–Zn coordination number. For this purpose, only Pd atoms on the (111) faces of the particle were considered where the maximum possible Pd–Zn surface coordination in the surface plane was 6. The (111) faces represented 67% of the total exposed surface area. The remaining surface area was composed of (100) faces (14%), edge atoms (17%), and corner atoms (2%). Table 4 summarizes of the abundance of the different Pd sites on the (111) face of the nanoparticle. We recognize that in the ordered 1:1 PdZn intermetallic present on the ZnO-supported sample (1PdZnO) the Zn atoms should not follow a random arrangement, but rather

Table 4
Type and number of sites present on the (111) face of a 4033 atom cubo-octahedral Pd nanoparticle. The nomenclature Pd–(Pd)*x*(Zn)*y* represents a Pd site with *x* Pd and *y* Zn nearest neighbors along the (111) face

	Pd–(Pd)6(Zn)0	Pd–(Pd)5(Zn)1	Pd–(Pd)4(Zn)2	Pd–(Pd)3(Zn)3	Pd–(Pd)2(Zn)4	Pd–(Pd)1(Zn)5	Pd–(Pd)0(Zn)6
2Pd0Zn	728	0	0	0	0	0	0
2Pd2Zn	131	217	150	58	11	2	0
2Pd6Zn	49	140	160	106	39	5	0
2Pd10Zn	37	119	160	114	46	8	1
2Pd14Zn	34	113	158	116	48	9	1
2Pd19Zn	17	76	130	131	71	14	1
1PdZnO	3	24	77	124	110	36	4

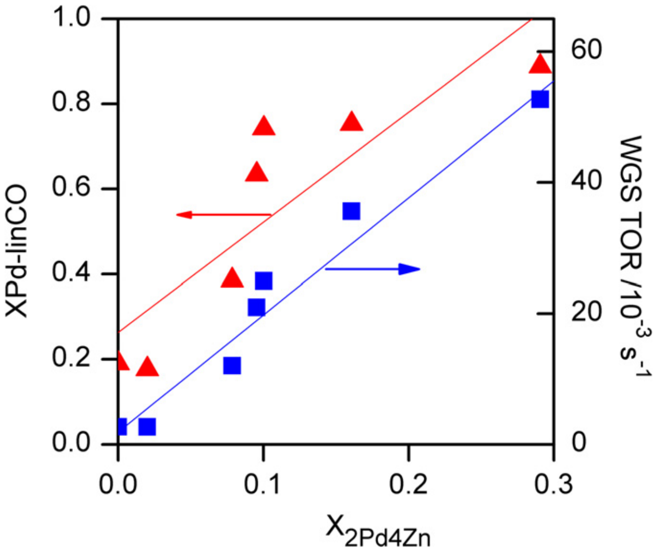

Fig. 7. (▲) Correlation between the fraction of Pd bound linearly to CO ($X_{\text{Pd-linCO}}$) as measured experimentally by DRIFTS and the fraction of Pd with 4 Zn coordination on the surface of the PdZn nanoparticle as estimated by the random sampling model (X_{Pd4Zn}). Also, (■) WGS TOR as a function of X_{Pd4Zn}.

should be ordered; however, our simple model predicted that an average Pd–Zn coordination number of 5.9 (measured experimentally for the PdZn alloy) corresponded to a bulk Zn/Pd ratio of 0.99, in good agreement with the Zn/Pd = 1 expected for the 1:1 PdZn intermetallic. Therefore, for consistency, we used the results of the random sampling for sample 1PdZnO despite the nonrandom nature of its structure. Because no surface or bulk segregation effects were taken into consideration, the deviation between the resulting percentage of Zn on the surface and in the bulk was <3%.

From the results in Table 4, it is clear that Pd atoms surrounded by 0, 1, or 2 Zn atoms were not the sites responsible for the increase in WGS TOR, because the number of these sites decreased, rather than increased, with Zn loading. Although largely abundant, the number of Pd sites with 3 Pd and 3 Zn neighbors did not change significantly for samples with ⩾6% Zn; therefore, the abundance of this site in and of itself cannot explain the increase in the rate data. Fig. 7 shows the correlation between the WGS TOR and the fraction of Pd that is on the surface and has a Pd–Zn coordination number of 4 according to the random sampling model. The trend suggests that the abundance of Pd centers with 4 Zn and 2 Pd neighbors correlates best with the WGS reaction rate on the PdZn catalysts. This model of the PdZn surface assumes that the TOR for the sites with 0, 1, 2 and 3 Zn neighbors was smaller than that of Pd centers with 4 Zn neighbors. The correlation between the fraction of Pd with a Zn coordination number of 5 or 6 and the WGS rate was lower than that with a Zn coordination number of 4. The sites with a Zn coordination number of 5 were only 25% of those with a Zn coordination number of 4, and the sites with a Zn coordination number of 6 were very rare. This suggests that the TOR for the 5 and 6 coordination sites was not much different than that for 4 coordination site. Note that the foregoing model assumes that only the surface geometry is important; for example, we do not take into account any Zn in the second layer that interacts with the Pd on the surface. Periodic DFT calculations [24] have identified the (111) surface of 1:1 PdZn bimetallic as the most stable. This closely packed surface is composed of alternating rows of Pd and Zn atoms, with all of the Pd atoms surrounded by 2 Pd and 4 Zn neighbors. Thus, our model is in agreement with these *ab initio* calculations, and suggests that enhanced WGS TOR is related to the presence of this surface moiety. Although the PdZn nanoparticle model yields a trend between TOR and surface composition, it does not provide a conclusive evidence that the proposed Pd site is the actual active site.

One possible explanation for the high TOR for the PdZn intermetallic comes from the work of Rodriguez [28], who showed that the electronic perturbation to the Pd atom caused by the formation of the Pd–Zn alloy reduces the ability of Pd to adsorb CO by transferring electrons from Pd to Zn. The weakened Pd–CO interaction could be partially responsible for the shift in adsorption geometry for CO on Pd; however, we believe that this weakened Pd–CO interaction is not the main driver of the enhanced WGS TOR, because we found no significant change in the apparent reaction order with respect to CO (see Table 3). Interestingly, we did note a significant change in the apparent reaction order with respect to CO_2. It is interesting that several studies [23,25,26] have shown that the Pd 4d local density of states (LDOS) for the PdZn alloy appears more like the LDOS of Cu than that of Pd. Coincidentally, Cu has also larger WGS TOR than Pd [53], as well as a −0.6 reaction order with respect to CO_2.

The inset in Fig. 5 shows a trend between the fraction of Pd that binds CO linearly ($X_{\text{Pd-linCO}}$) and the WGS TOR. The slope of the line is our best estimate of the true TOR and is the same for all samples; therefore, a correlation between $X_{\text{Pd-linCO}}$ and the fraction of Pd sites with 4 Zn coordination also would be expected, as is shown in Fig. 7. Consequently, the fraction of Pd that binds CO linearly is correlated with the fraction of Pd atoms with 4 Zn neighbors and not with the fraction of surface Pd atoms that are completely isolated (Table 4). This finding implies that although some Pd–Pd neighbors are available, CO still binds mostly in a linear fashion. We have no explanation for the shift in CO adsorption geometry. In a density functional study, Chen et al. [45] found similar binding energies of linear and bridging CO on PdZn (111) (∼96 kJ mol^{-1}), implying that similar surface coverages can be expected for both species. In comparison, the 1:1 PdZn catalyst (1PdZnO) studied here had about 9 times more linear CO adsorbed than bridging CO under WGS conditions. Here we note that during the *in situ* IR experiments, the ratio of linear to bridging CO exhibited large but reversible changes depending on the conditions (i.e., temperature and gas composition). More precisely, the linear-to-bridge CO ratio was decreased at low temperatures and in the absence of H_2 (data not shown). Therefore, the DFT results are not in direct contradiction with our findings, because the binding energies were calculated at zero temperature and pressure. It is also possible that the presence of H_2O, H_2, and CO_2 and their respective surface intermediates hinders the adsorption of bridging CO. The Chen et al. study found that C-species, such as atomic C, CO, and CH_3, were bound preferentially to Pd over PdZn, whereas O-species, such as atomic O and CH_3O, bind more strongly to PdZn than to Pd, due to the greater affinity between Zn and O. Such a trend would suggest that PdZn plays an important role in the activation of H_2O, which is believed to be the rate-limiting step for the WGS reaction. A subsequent study by Lim et al. [54] calculated the binding energies of H_2O and its intermediates (O, H, OH) on PdZn. As expected, O and OH were found to bind more strongly to Zn-rich sites on the PdZn (111) surface. In comparison, there is no experimental evidence to suggest that H_2O dissociates on clean Pd (111) surface, whereas the dissociation of H_2O on Pt (111) is highly endothermic (68 $\text{kJ}\,\text{mol}^{-1}$) [55]. This suggests not only that PdZn stabilizes the dissociation of H_2O, but also that it may stabilize other possible WGS intermediates, such as formates, carbonates, and carboxyls. Proving this hypothesis will require additional *ab initio* calculations.

4.4. Particle dispersion and Zn availability to form PdZn alloy

The particle size (in nm) can be estimated by taking the reciprocal of the measured metal dispersion [56]. The estimated particle size was 4 nm for the pure Pd on alumina sample. The particle sizes for the remaining samples were estimated from the corresponding Pd dispersions measured by O_2–H_2 titration; particle sizes were between 3 and 5 nm. The only exception was the sample with 19% Zn loading, which had a dispersion of 0.08. But we believe that this low dispersion value does not represent the true Pd dispersion under reaction conditions, for two reasons. First, if 0.08 were the actual Pd dispersion, then the metal particles would be about 12 nm in diameter. Such large particles should have a total coordination number ($N_{\text{Pd–Pd}} + N_{\text{Pd–Zn}}$) close to the bulk coordination number of 12. But the measured total coordination number for sample 2Pd19Zn ($N_{\text{Pd–Pd}} + N_{\text{Pd–Zn}} = 6.3$) was far from this value. Moreover, because the O_2 uptake for this sample was similar to that for the other catalysts, whereas the H_2 uptake was at least a factor of 2 smaller, then the Zn/Pd ratio in the particle should be large ($\sim$4.2), which in turn would yield a high Pd–Zn coordination number. Second, this sample was the only one with XRD data demonstrating the presence of bulk ZnO. It is plausible that Zn was oxidized by O_2 forming ZnO particles, which moved on top of Pd particles, blocking Pd sites. As discussed earlier, under reaction conditions, ZnO can be reduced and can move away from the particles. When H_2 chemisorption preceded by a 4-h reduction at 300 °C was performed on sample 2Pd19Zn, the measured Pd dispersion increased to 0.20, indicating that the reduced Zn atoms can move away from Pd particles.

Based on the random sampling model discussed earlier (Section 4.3), we could estimate the Zn/Pd ratio in the PdZn particles required to match the average Pd–Zn coordination number obtained by EXAFS. The results for the various samples were 0.3 for 2Pd2Zn, 0.4 for 2Pd6Zn, 0.5 for 2Pd10Zn, 0.5 for 2Pd14Zn, 0.7 for 2Pd19Zn, and 1.0 for 1PdZnO. The agreement between the Zn/Pd ratios reported here and those estimated from the O_2 and H_2 uptakes (Table 1) was not good. The main reason for the inconsistency was the presence of reduced Zn on the surface of the support in addition to Zn on the surface of the Pd–Zn particles. When O_2 was dosed over the sample during the chemisorption measurements, it reacted with Pd and both types of Zn atoms (Zn in alloy, Zn on support), leading to the large Zn/Pd ratios reported Table 1. The amount of reduced Zn on the support would be expected to increase with increasing Zn loading. In agreement with this idea, the deviation between Zn/Pd reported earlier and in Table 1 was greater for the samples with high Zn loadings (i.e., 10%, 14%, and 19%).

Knowing the Zn/Pd ratio in the metallic particles and the metal loadings of the catalysts, and assuming that the Zn not in the alloy reacts with the support, allows the estimation of Zn in the $ZnAl_2O_4$ phase. For a Zn/Pd ratio of 0.3, 85% of the added Zn formed $ZnAl_2O_4$. As the Zn loading increased, the percentage of Zn in the form of $ZnAl_2O_4$ grew to 91%, 94%, 95%, and 96% for the remaining Pd/Zn/Al_2O_3 samples. Therefore, at least 85% of the Zn added to the catalyst reacted with the support to form $ZnAl_2O_4$. The formation of $ZnAl_2O_4$ from mixtures of alumina and ZnO has been reported previously. However, the formation of this phase required calcination at temperatures above 800 °C [57–59]. Formation of $ZnAl_2O_4$ also has been reported at 650 °C, but only under hydrothermal treatment of Al_2O_3/ZnO mixtures [60]. Zawadzki et al. [61] reported the formation of the aluminate under hydrothermal treatment at 180 °C followed by calcination of the resulting gel at 600 °C, with zinc acetate and aluminum nitrate as the sources of the metals. Scott et al. [62] showed that H_2 treatment at 350 °C did not yield the aluminate in Al_2O_3/ZnO mixtures. Consequently, we believe that under the conditions considered here (250–350 °C and >25% H_2), the presence of Pd catalyzed the formation of $ZnAl_2O_4$. Although we could not measure it for our catalysts, the surface area of $ZnAl_2O_4$ was estimated to be about 73 $\text{m}^2\,\text{g}^{-1}$ by assuming that all of the added Zn reacted with the Al_2O_3 support to form a separate phase, and that the total surface area was equal to the sum of the surface area of the Al_2O_3 and $ZnAl_2O_4$ phases. This specific surface area for $ZnAl_2O_4$ is not unreasonable; Zawadzki et al. [61] measured a BET area of 85 $\text{m}^2\,\text{g}^{-1}$ for a $ZnAl_2O_4$ sample calcined at temperatures below 600 °C.

IR data showed that as the Zn loading increased, the intensity of the features in the 1592–1392 cm^{-1} region belonging to carbonates also increased. The absence of any features in that region of the DR spectra for Pd/ZnO suggests that these carbonates species were located on the alumina support or at the metal–support interface. The XRD data in Fig. 2 show that the amount of $ZnAl_2O_4$ also increased with Zn loading. Therefore, we believe that the increase in IR intensity in the 592–1392 cm^{-1} region is related to the increased stability of the carbonate species on $ZnAl_2O_4$ compared with Al_2O_3. These data suggest an alternative explanation for the effect of Zn. The linear increase in the amount of $ZnAl_2O_4$ with the amount of Zn may imply that the interaction between Pd and alumina also will decrease as the alumina is transformed to the aluminate. If a strong Pd–alumina interaction were to lead to a decreased TOR of Pd, then the addition of Zn would have the effect of avoiding this interaction. Thus Zn could have two effects: the formation of PdZn alloys, as discussed in detail above, and a reaction with alumina, thereby weakening the Pd–alumina interaction and freeing the Pd to act in its more purely metallic state. The challenge to this picture is rationalizing a strong Pd–alumina interaction when the average Pd particle diameter is 4 nm.

The TORs for samples 2Pd6Zn and 2Pd6Zn500 were $(12 \pm 1) \times 10^{-3}$ and $(13 \pm 1) \times 10^{-3}$ $\text{mol}\,H_2\,\text{s}^{-1}$ (mol exposed Pd)$^{-1}$, respectively. The higher reduction temperature of 500 °C for 2 h (sample 2Pd6Zn500) did not increase the extent of Pd–Zn interaction, suggesting that all of the available Zn was already trapped by the alumina at 300 °C. For these samples, the zinc nitrate precursor was added through the incipient wetness method, producing a finely dispersed Zn phase on the support that likely was in close contact with the Pd particles. In contrast, when the Zn was added as ZnO physically mixed with the supported Pd catalyst (samples 2Pd6ZnPM and 2Pd6ZnPM500), the reduction temperature played a key role in the extent of Pd–Zn interaction. As discussed in Section 3.4, the WGS and methanation TORs for the sample reduced at 300 °C (2Pd6ZnPM) were similar to those for pure Pd on Al_2O_3, whereas the WGS and methanation TORs for the sample reduced at 500 °C (2Pd6ZnPM500) were similar to those for 2Pd6Zn. As supported by EXAFS (see Section 3.2), the Zn was able to find and react with Pd at 500 °C but not at 300 °C. Compared with the finely dispersed Zn precursor obtained by impregnation, the process of moving Zn from the precursor to the Pd particles is more complex for the physical mixture. ZnO reduction must occur first. The resulting Zn^0, which has a high vapor pressure, must diffuse into the alumina via gas-phase transport before it can reach the Pd and react. Many of the Zn^0 atoms are deposited on the surface of the alumina support instead of reacting with Pd particles, as supported by the chemisorption data in Table 1. The Zn/Pd ratio estimated from the O_2 and H_2 uptake was 1.5 for the physical mixture sample (2Pd6ZnPM500). In comparison, samples 2Pd6Zn and 2Pd6Zn500 had Zn/Pd ratios of 0.6 and 1.1, respectively, suggesting that more Zn was available on the surface of the physical mixture sample. In addition, XRD (data not shown) also demonstrated the presence of $ZnAl_2O_4$ in sample 2Pd6ZnPM500. The physical mixture samples likely produced particles with a nonuniform Pd/Zn distribution.

5. Conclusion

In this study, alumina-supported Pd samples were prepared with six Zn loadings. The extent of alloy formation increased with the amount of Zn added; however, >85% of the Zn reacted with alumina to form zinc aluminate, leaving only a small fraction of Zn available to react with Pd. At 280 °C and 1 atm (6.8% CO, 8.5% CO_2, 37% H_2O, 37.4% H_2), the TOR for the sample with 19% Zn added was increased by a factor of 13, to 3.6×10^{-2} mol H_2 s^{-1} (mol exposed Pd)$^{-1}$, compared with the pure metallic Pd supported on alumina. The average Pd–Zn coordination number increased from 0 to 4.5 for Zn loadings between 0 and 19%, indicating the formation of a Pd–Zn alloy. The formation of an ordered 1:1 PdZn intermetallic compound on ZnO increased the WGS turnover rate by a factor of 20 to 5.3×10^{-2} mol H_2 s^{-1} (mol exposed Pd)$^{-1}$; the corresponding average Pd–Zn coordination number was 5.9. Based on *in situ* diffuse reflectance infrared spectroscopy, we observed that as the extent of alloy formation increased, the adsorbed CO on Pd switched from a bridging conformation to a linear conformation. In agreement with infrared data, a simple random substitution model for PdZn alloy formation suggested that Pd sites surrounded by 4 Zn and 2 Pd were necessary to change the adsorption conformation of CO from bridge to linear. The same random substitution model showed that Pd atoms on the surface with this coordination correlated best with the rate per surface Pd for WGS catalysis. We also note that a strong interaction of Pd with alumina could make it less effective as a WGS catalyst. In that case, the role of Zn is twofold; it can form the PdZn alloy and also can react with the alumina and weaken the interaction of Pd with the resulting support. Thus, as the amount of Zn is increased, the Pd interaction with alumina is decreased. Whereas the beneficial effect of Zn addition to Pd/Al_2O_3 is clear, the relative impact on the rate per Pd atom of alloy formation versus weakening of the Pd support interaction requires further investigation on systems with more weakly interacting supports.

Acknowledgments

Support for this research was provided by the U.S. Department of Energy, Office of Basic Energy Sciences, through Catalysis Science grant DE-FG02-03ER15466. Use of the Advanced Photon Source was supported by the U.S. Department of Energy, Office of Science, Office of Basic Energy Sciences under contract DE-AC02-06CH11357. The authors thank the National Science Foundation for a Major Research Instrumentation grant (MRI award 0321118-CTS) that was used to establish the Laboratory for In-situ X-ray Scattering from Nanomaterials and Catalysts, in which the diffraction data were collected.

Supporting material

The online version of this article contains additional supplementary material.

The supplemental information includes the *in situ* DRIFTS spectra in the region of 1700–1200 cm^{-1} showing the presence of formates and carbonates species on the surface of the support.

Please visit DOI: 10.1016/j.jcat.2008.04.005.

References

[1] R. Farrauto, S. Hwang, L. Shore, W. Ruettinger, J. Lampert, T. Giroux, Y. Liu, O. Ilinich, Annu. Rev. Mater. Res. 33 (2003) 1–27.
[2] D.S. Newsome, Catal. Rev. Sci. Eng. 21 (1980) 275–318.
[3] J.R. Ladebeck, J.P. Wagner, in: W. Vielstich, A. Lamm, H.A. Gasteiger (Eds.), Handbook of Fuel Cells—Fundamentals, Technology and Applications, Wiley & Sons, Chichester, 2003, pp. 190–201.
[4] T. Bunluesin, R.J. Gorte, G.W. Graham, Appl. Catal. B 15 (1998) 107–114.
[5] R.J. Gorte, S. Zhao, Catal. Today 104 (2005) 18–24.
[6] G. Jacobs, A.C. Crawford, B.H. Davis, Catal. Lett. 100 (2005) 147–152.
[7] G. Jacobs, U.M. Graham, E. Chenu, P.M. Patterson, A. Dozier, B.H. Davis, J. Catal. 229 (2005) 499–512.
[8] G. Jacobs, S. Khalid, P.M. Patterson, D.E. Sparks, B.H. Davis, Appl. Catal. A 268 (2004) 255–266.
[9] A.A. Phatak, N.A. Koryabkina, S. Rai, J.L. Ratts, W. Ruettinger, R. Farrauto, G.E. Blau, W.N. Delgass, F.H. Ribeiro, Catal. Today 123 (2007) 224–234.
[10] K. Takahashi, H. Kobayashi, N. Takezawa, Chem. Lett. (1985) 759–762.
[11] N. Takezawa, N. Iwasa, Catal. Today 36 (1997) 45–56.
[12] J. Agrell, G. Germani, S.G. Jaras, M. Boutonnet, Appl. Catal. A 242 (2003) 233–245.
[13] Y.H. Chin, R. Dagle, J.L. Hu, A.C. Dohnalkova, Y. Wang, Catal. Today 77 (2002) 79–88.
[14] Y.H. Chin, Y. Wang, R.A. Dagle, X.H.S. Li, Fuel Process. Technol. 83 (2003) 193–201.
[15] M.L. Cubeiro, J.L.G. Fierro, J. Catal. 179 (1998) 150–162.
[16] N. Iwasa, S. Kudo, H. Takahashi, S. Masuda, N. Takezawa, Catal. Lett. 19 (1993) 211–216.
[17] N. Iwasa, S. Masuda, N. Ogawa, N. Takezawa, Appl. Catal. A 125 (1995) 145–157.
[18] N. Iwasa, T. Mayanagi, S. Masuda, N. Takezawa, React. Kinet. Catal. Lett. 69 (2000) 355–360.
[19] N. Iwasa, T. Mayanagi, W. Nomura, M. Arai, N. Takezawa, Appl. Catal. A 248 (2003) 153–160.
[20] A. Karim, T. Conant, A. Datye, J. Catal. 243 (2006) 420–427.
[21] Y.H. Wang, J.C. Zhang, H.Y. Xu, Cuihua Xuebao 27 (2006) 217–222.
[22] Y.H. Wang, J.C. Zhang, H.Y. Xu, X.F. Bai, Cuihua Xuebao 28 (2007) 234–238.
[23] A. Bayer, K. Flechtner, R. Denecke, H.P. Steinruck, K.M. Neyman, N. Rosch, Surf. Sci. 600 (2006) 78–94.
[24] Z.X. Chen, K.M. Neyman, A.B. Gordienko, N. Rosch, Phys. Rev. B Condens. Matter Mater. Phys. 68 (2003) 075417.
[25] K.M. Neyman, K.H. Lim, Z.X. Chen, L.V. Moskaleva, A. Bayer, A. Reindl, D. Borgmann, R. Denecke, H.P. Steinruck, N. Rosch, Phys. Chem. Chem. Phys. 9 (2007) 3470–3482.
[26] A.P. Tsai, S. Kameoka, Y. Ishii, J. Phys. Soc. Jpn. 73 (2004) 3270–3273.
[27] G. Xia, J.D. Holladay, R.A. Dagle, E.O. Jones, Y. Wang, Chem. Eng. Technol. 28 (2005) 515–519.
[28] J.A. Rodriguez, J. Phys. Chem. 98 (1994) 5758–5764.
[29] J.E. Benson, M. Boudart, J. Catal. 4 (1965) 704.
[30] J.E. Benson, H.S. Hwang, M. Boudart, J. Catal. 30 (1973) 146–153.
[31] J. Sirita, S. Phanichphant, F.C. Meunier, Anal. Chem. 79 (2007) 3912–3918.
[32] C.T. Hong, C.T. Yeh, F.H. Yu, Appl. Catal. 48 (1989) 385–396.
[33] N. Iwasa, N. Ogawa, S. Masuda, N. Takezawa, Bull. Chem. Soc. Jpn. 71 (1998) 1451–1455.
[34] D. Brennan, D.O. Hayward, B.M.W. Trapnell, Proc. R. Soc. London A 256 (1960) 81–105.
[35] X.C. Guo, A. Hoffman, J.T. Yates, J. Chem. Phys. 90 (1989) 5787–5792.
[36] Pd, ICDD card # 46-1043.
[37] $ZnAl_2O_4$, ICDD card # 05-0669.
[38] ZnO, ICDD card # 36-1451.
[39] PdZn, ICDD card # 06-0620.
[40] W.B. Pearson, Pearson's Handbook of Crystallographic Data for Intermetallic Phases, American Society for Metals, Metals Park, 1985.
[41] O.P. Tkachenko, A.Y. Stakheev, L.M. Kustov, I.V. Mashkovsky, M. van den Berg, W. Grunert, N.Y. Kozitsyna, Z.V. Dobrokhotova, V.I. Zhilov, S.E. Nefedov, M.N. Vargaftik, I.I. Moiseev, Catal. Lett. 112 (2006) 155–161.
[42] R.P. Eischens, W.A. Pliskin, Adv. Catal. 10 (1958) 1–56.
[43] K.I. Choi, M.A. Vannice, J. Catal. 131 (1991) 1–21.
[44] E. Jeroro, V. Lebarbier, A. Datye, Y. Wang, J.M. Vohs, Surf. Sci. 601 (2007) 5546–5554.

[45] Z.X. Chen, K.M. Neyman, K.H. Lim, N. Rosch, Langmuir 20 (2004) 8068–8077.

[46] R.A. Dallabetta, M. Shelef, J. Catal. 48 (1977) 111–119.

[47] Y. Amenomiya, J. Catal. 57 (1979) 64–71.

[48] P.G. Gopal, R.L. Schneider, K.L. Watters, J. Catal. 105 (1987) 366–372.

[49] G. Busca, J. Lamotte, J.C. Lavalley, V. Lorenzelli, J. Am. Chem. Soc. 109 (1987) 5197–5202.

[50] A.A. Davydov, Infrared Spectroscopy of Adsorbed Species on the Surface of Transition Metal Oxides, John Wiley & Sons, New York, 1990, p. 243.

[51] M.A. Vannice, S.Y. Wang, J. Phys. Chem. 85 (1981) 2543–2546.

[52] N.A. Koryabkina, A.A. Phatak, W.F. Ruettinger, R.J. Farrauto, F.H. Ribeiro, J. Catal. 217 (2003) 233–239.

[53] D.C. Grenoble, M.M. Estadt, D.F. Ollis, J. Catal. 67 (1981) 90–102.

[54] K.H. Lim, L.V. Moskaleva, N. Rosch, ChemPhysChem 7 (2006) 1802–1812.

[55] S. Kandoi, A.A. Gokhale, L.C. Grabow, J.A. Dumesic, M. Mavrikakis, Catal. Lett. 93 (2004) 93–100.

[56] M. Boudart, Kinetics of Heterogeneous Catalytic Reactions, Princeton University Press, Princeton, 1984.

[57] G. Aguilar-Rios, M.A. Valenzuela, H. Armendariz, P. Salas, J.M. Dominguez, D.R. Acosta, I. Schifter, Appl. Catal. A 90 (1992) 25–34.

[58] M.C. Marion, E. Garbowski, M. Primet, J. Chem. Soc. Faraday Trans. 87 (1991) 1795–1800.

[59] H. Zou, J.Y. Shen, Thermochim. Acta 351 (2000) 165–170.

[60] Y. Nagamori, M. Kawase, Microporous Mesoporous Mater. 21 (1998) 439–445.

[61] M. Zawadzki, W. Mista, L. Kepinski, Vacuum 63 (2001) 291–296.

[62] S.P. Scott, M. Sweetman, J. Thomson, A.G. Fitzgerald, E.J. Sturrock, J. Catal. 168 (1997) 501–510.